ROYAL SOCIETY
OF CHEMISTRY

PAPER

An ultra-fast-charging and long-cycling titanium niobate/reduced graphene oxide anode *via* electrophoretic interfacial engineering

Fan Yu, [iD] Yihan Wang, Nicolas Brodusch, Bobby Miglani, [iD] Nauman Mubarak, Jinhyuk Lee, [iD] Raynald Gauvin and George P. Demopoulos [iD] *

Titanium niobate (TiNb$_2$O$_7$, TNO) materials are emerging as high-performing anode candidates for fast charging Li-ion batteries. However, the non-homogeneous interfacial electrode microstructure, which directly affects electrochemical kinetics, electrode structural stability, and volume variation, results in significant performance loss upon extended cycling under fast charging. To address these issues, we have nanoengineered a carbon-coated single-crystal Fe-doped TNO (C-FeTNO)/reduced graphene oxide (rGO) anode with ultra-fast (5C) capability over 5000 cycles. This is achieved *via* electrophoretic deposition (EPD) controlled at the nanoscale with graphene oxide acting as a binder and conductive component upon reduction annealing. The designed electrode exhibits a dramatic reduction in charge transfer impedance from 183 ohms to 75 ohms and boosting of the Li ion diffusion coefficient by one order of magnitude from 10^{-12} to 10^{-11} cm^2 s^{-1}. Consequently, the EPD nanoengineered TNO/rGO hybrid anode demonstrates outstanding performance, namely capacities of 252, 246, 236, and 210 mAh g^{-1} at 0.5C, 1C, 2C, and 5C, respectively. More remarkably, it is shown to have exceptional cycling stability with 70% retention after 5000 cycles at 5C. This remarkable electrochemical performance can be attributed to the EPD-enabled nanoscale interfacial contact (between C-coated Fe-TNO and rGO) and the homogeneous microstructure endowing the electrode with a highly conductive and stable charge percolation network.

1. Introduction

Electric vehicles (EVs) require ultrafast-charging lithium-ion batteries (LIBs) with high capacity and long cycle life.[1–4] For such applications, extremely fast charging (XFC) LIBs have been identified as those reaching 80% state of charge in less than 15 minutes (>4C fast charging) while maintaining high capacity retention after a decade of usage.[1] However, traditional anode materials, *i.e.*, graphite with a low working potential (*ca.* 0.1 V (*vs.* Li/Li$^+$)), are not suitable for such applications as due to the developed polarization under extremely fast charging, lithium plating is triggered leading to short circuiting and battery failure.[5] Meanwhile, a commercial Li$_4$Ti$_5$O$_{12}$ anode provides superior fast-charging capacity, safe working voltage, and long cycle life, but it suffers from low theoretical capacity (only 175 mAh g^{-1}).[6] Therefore, it is urgent to explore next-generation fast-charging anode materials.

Titanium niobate (TiNb$_2$O$_7$, TNO) has emerged as a promising candidate, offering fast ionic diffusion kinetics, high theoretical capacity, and safe working potential.[7–9] However, its application suffers from significant capacity fade after long-term cycling under fast-charging conditions due to poor electronic conductivity, crystal structure change, and unwanted insulating layer formation.[7,9] To address this issue, both the bulk material structure and the interphase need to be improved. The former can be modified by crystal control during nanomaterial synthesis, element doping, *etc.*[7,10–14] Specifically, the single-crystal structure of TNO offers continuous Li ion diffusion pathways along well-defined crystallographic planes, while nanosizing can shorten diffusion pathways – both contributing to ionic kinetics.[10–12,14] Additionally, elemental doping can further widen diffusion channels, improve structural stability, and modulate the band gap, thereby promoting fast-charging and cycling performance.[7,11,15,16] For example, our previous study demonstrated that Fe^{3+} substitution in single-crystal TNO nanostructures crystallographically extends the *ac*-plane, suggesting widened diffusion channels along the transport pathway.[16] Consequently, this structural change reduces the Li-ion hopping energy barrier and increases the diffusion coefficient. Also, Fe^{3+} substitution modulates the band gap to increase electronic conductivity, and introduces Fe–O bonds to improve structural stability.[16] The latter can be improved by constructing conductive percolation networks *via* advanced electrode/interphase engineering.[14,17–19] While only a few studies have explored this direction, the synergy between these

Materials Engineering, McGill University, 3610 rue University, Montreal, QC H3A 0C5, Canada. E-mail: george.demopoulos@mcgill.ca

This journal is © The Royal Society of Chemistry 2025

J. Mater. Chem. A, 2025, **13**, 32207–32219 | **32207**

strategies opens a promising path toward designing ultra-fast charging and long-cycling TNO anodes.[7] Towards this goal, rationally built three-dimensional fast-ionic/electronic networks consisting of cation-doped TNO single crystals and graphene are considered a potentially rewarding strategy in this context.[16,20] This novel electrode design approach leverages the multifunctionality of graphene, including excellent electronic conductivity, mechanical/thermal stability, Li-storage capability, and binding properties, which can enhance kinetics, suppress volume variation, and prevent electrolyte decomposition.[13,21] However, traditional electrode engineering and interphase control approaches encounter several obstacles in fabricating such 3D graphene/TNO electrodes with well-defined interphases. Conventional battery electrode manufacturing involves tape casting (or blade coating) a suspension made of organic solvent, carbon, binder, and an active material, followed by drying under oxygen-exposed conditions. This process often leads to the oxidation of graphene, transforming the highly-conductive graphene material into a low-conductivity phase.[22] Additionally, nonhomogeneous coating processes lead to significant aggregation of nanomaterials and non-uniform electrode–electrolyte interphase formation, which causes severe polarization and subsequent battery degradation.[19,20] Also, non-active components including the conductive carbon and binder limit the available capacity and volumetric electrode energy density.[23] Moreover, the use of toxic solvents like NMP (N-methyl pyrrolidone) raises safety and environmental concerns.[19,24] Thus, an alternative electrode engineering process that can achieve a uniform electrode interfacial microstructure for high performance via environmentally friendly means is of great urgency.

Electrophoretic deposition (EPD) technology, as an advanced electrode engineering and interphase control technique, is known for its superior uniformity, low cost, equipment simplicity, and high scalability.[25–27] Recent studies have shown that the EPD approach outperforms the conventional tape casting method in constructing TNO/reduced graphene oxide (rGO) composite electrodes with high capacity and a uniform interface.[28,29] For example, Uceda et al.[19] electrophoretically co-deposited micron-sized TNO particles and rGO to engineer a binder-free all-active-material LIB electrode with a highly homogeneous percolation network but its cycling retention and rate performance were not satisfactory because the TNO material used obtained via solid-state calcination and milling was coarse and full of defects. In addition, the precise control of electrode composition and mass loading is still difficult to be realized. Therefore, developing high-performance TNO/rGO composite materials via EPD constitutes a yet unexplored but highly promising advanced electrode engineering avenue.

Herein, we describe the EPD-enabled design of a carbon-coated Fe-doped single-crystal TNO nanomaterial/rGO advanced electrode structure with unparalleled ultra-fast charging and long-cycling performance. Thanks to the nanoscale assembling properties of EPD the fabricated electrodes are characterized by excellent composition homogeneity boasting significantly reduced impedance and a very high Li-ion diffusivity network. At the electrode level, this EPD anode offers

remarkable rate performance, showing capacities of 252, 246, 236, and 210 mAh g^{-1} at 0.5C, 1C, 2C, and 5C, respectively, and demonstrates excellent cycling retention of 70% after 5000 cycles at 5C.

2. Experimental section

2.1. Synthesis of nanostructured Fe-doped TNO (FeTNO)

The single-crystal Fe-substituted TNO nanomaterial (Fe$_{0.05}$-Ti$_{0.95}$Nb$_2$O$_{6.975}$, FeTNO) was synthesized using a universal and scalable approach featuring co-precipitation and high-temperature calcination (Scheme S1(a)), as described in our previous research.[14,16] Three feedstock aqueous colloidal solutions were prepared via temperature-controlled partial hydrolysis (under 10 °C) of ferric chloride hexahydrate (FeCl$_3\cdot$6H$_2$O, 99%, Sigma-Aldrich, USA), titanium tetrachloride (TiCl$_4$, 99.0%, Sigma-Aldrich, USA), and niobium pentachloride (NbCl$_5$, 99%, Thermo Fisher Scientific, USA). By mixing these three feedstock solutions, the composite Fe–Ti–Nb–Cl solution was prepared containing 0.000125 mol L^{-1} Fe(III), 0.02375 mol L^{-1} Ti(IV), and 0.05 mol L^{-1} Nb(V). The latter solution was neutralized by dropwise adding ammonium hydroxide (99.9% NH$_4$OH, 29% NH$_3$ basis, Sigma-Aldrich, USA) inducing hydrolytic co-precipitation of a nanosized FeTNO intermediate. After washing and drying, the FeTNO precursor was crystallized at 900 °C for 4 hours in a continuous flow of oxygen gas with a heating ramping rate of 5 °C min^{-1} in a tube furnace oven (OTF-1200X-S50-2F Mini CVD tube furnace, MTI Corporation, USA).

2.2. Carbon coating of FeTNO (for C-FeTNO)

Carbon coating of FeTNO was conducted by the high-temperature decomposition of a lactose carbon precursor (Scheme S1(a)), as reported previously.[19] Then 1 g of the FeTNO material was mixed with 5 mL lactose aqueous solution (22.4 g L^{-1} lactose), followed by drying at 120 °C in an oven. The carbon-coated FeTNO material (C-FeTNO) was obtained by annealing at 700 °C for 400 minutes in a tube furnace oven under a pure argon atmosphere.

2.3. Electrophoretic deposition of the C-FeTNO/rGO electrode

As shown in Scheme S1(b), the electrode was engineered by electrophoretically co-depositing C-FeTNO and GO on Al foil immersed in an isopropanol suspension. After deposition, the EPD prepared electrode was subjected to thermal treatment in the presence of H$_2$ so GO is reduced and the C-FeTNO/rGO anode is constructed. The optimal parameters of the process have been investigated as discussed below.

2.3.1. Suspension preparation. The optimal EPD suspension contains 66.7 mL of pure isopropanol solvent, 184 mg of C-FeTNO, 16 mg of graphene oxide (GO, Sigma-Aldrich, powder, 15–20 sheets), and 66 ppm of lithium acetate (LiOAc, Sigma-Aldrich, 99%) added as a charging agent. This suspension makeup corresponds to 3 g L^{-1} solid loading and a mass ratio of 92/8 of C-FeTNO/GO between C-FeTNO and GO. In establishing

32208 | J. Mater. Chem. A, 2025, **13**, 32207–32219

This journal is © The Royal Society of Chemistry 2025

the above suspension formulation different solvents were tested with and w/o prior C-coating or with or w/o charging additives. The different solvents tested are described in the S2 Section of the SI. The stability of suspensions was determined by settling tests (Fig. S1) and zeta potential measurements. In the suspension stability tests, 15 mg of solid particles (either GO or C-FeTNO) were added to 5 mL of different organic solvents, followed by sonication. These mixtures were then left to rest for 48 hours for visual inspection after 48 hours of resting.

2.3.2. EPD process for the C-FeTNO/GO film. An EPD electrolytic cell with a 15 μm Al foil working electrode and a stainless steel counter electrode was set up with an electrode spacing of 7.5 mm and a deposition area of 4 to 6 cm^2. Deposition occurred at the anode. The EPD cell was operated at different constant voltages (50 V, 100 V, and 200 V) supplied by a SourceMeter (Keithley 2611A) instrument.

2.3.3. Reduction for the C-FeTNO/rGO EPD electrode. The GO in C-FeTNO/GO films was reduced by annealing at 600 °C for 300 minutes in a 5 vol% H$_2$/Ar gas mixture to obtain the target C-FeTNO/rGO electrode composition.

2.4. Conventional electrode *via* tape casting

The reduction of GO samples was processed with the same procedure (as shown in Section 2.3.3) to obtain rGO. This rGO sample was applied to fabricate conventional electrodes.

In conventional electrode fabrication, a binder plus conductive carbon are used. Specifically, the active material, the conductive component (carbon black (CB)), and the polyvinylidene fluoride (PVDF) binder were mixed in a weight ratio of 8 : 1 : 1, and then added into *N*-methyl-2-pyrrolidone (NMP) solvent. After milling, this slurry was cast on the Al foil using a doctor blade before drying overnight.

To investigate the effects of different components, three electrodes were fabricated by the tape casting approach. The conventional FeTNO/CB/PVDF electrode consisted of the FeTNO material (active material), carbon black (conductive carbon), and PVDF binder, named the FeTNO electrode. To understand the carbon coating effect, C-FeTNO, carbon black, and PVDF binder were cast to fabricate the C-FeTNO/CB/PVDF electrode (namely, C-FeTNO electrode). Finally, the C-FeTNO/rGO/PVDF electrode was prepared by using C-FeTNO as the active material, rGO as a conductive agent, and PVDF as a binder. The component ratio was 8 : 1 : 1 on wt basis for all the formulations.

2.5. Material characterization

The elemental composition of Fe, Ti, and Nb in FeTNO samples and their concentrations in solutions were determined *via* inductively coupled plasma optical emission spectrometry (ICP-OES, Thermo scientific, iCAP 6700 Series). The crystal structures were determined by using a Bruker D8 Discover X-ray diffractometer (VANTEC Detector Cu-Source) and analysed *via* TOPAS (Bruker) V5 software. Attenuated total reflection Fourier transform infrared (ATR-FTIR) spectroscopy was carried out using an FTIR infrared spectrometer, Vertex 70, from Bruker. Raman microscopy was performed using a Thermo Scientific DXR2

Raman microscope, equipped with a DXR 532 nm wavelength laser. The morphology and elemental distribution of materials were determined using a Hitachi SU-8000 Cold Field-Emission scanning electron microscope (SEM) equipped with an energy-dispersive X-ray spectroscopy (EDS) detector (XMax 80 mm^2, Oxford Instruments). Cross-sectional SEM imaging and EDS mapping for the electrode film were performed with a Hitachi SU-9000 cold field-emission SEM/STEM instrument equipped with an Oxford Instruments windowless Extreme 100 mm^2 SDD detector. This setup is capable of achieving a resolution of 0.16 nm at 30 keV in BF mode and 0.4 nm in SE mode. Transmission electron microscopy (TEM), high-resolution transmission electron microscopy (HRTEM), scanning transmission electron microscopy (STEM), selected area electron diffraction (SAED), and fast fourier transform (FFT) imaging were performed on a Thermo Scientific Talos F200X G2 TEM/STEM instrument operated at 200 kV. Zeta potential, electrophoretic mobility, and suspension conductivity were measured using a Malvern Zetasizer Ultra (Malvern Instruments). To quantitatively determine the adhesion strength of the electrode film, a peel test was conducted using a ChemInstruments EZ Data 180° peel adhesive testing machine, operated at a peel speed of 5 cm min^{-1}.

2.6. Electrochemical characterization

Both EPD electrodes and conventional electrodes were assembled in half-cell batteries for electrochemical testing. Each coin cell consists of an electrode sheet, a lithium metal, a separator film (PP/PE/PP, Celgard 2325), and 200 μL of 1 M LiPF$_6$ in EC : DMC : DEC as electrolyte.

Battery charge–discharge cycling measurement and galvanostatic intermittent titration technique (GITT) analysis were carried out using a standard battery cycler (BT2043-10V-100 mA-40, Arbin) under different C rates (1C = 387.6 mAh g^{-1}) and in the voltage range between 3.0 V and 1.0 V. The same battery cycler instrument was also employed to perform potentiostatic intermittent titration technique (PITT) measurements. Cyclic voltammetry (CV) and electrochemical impedance spectroscopy (EIS) measurements were performed using a BioLogic VSP electrochemical workstation and analyzed by EC-Lab software.

For post-mortem analysis, the cycled battery electrodes of C-FeTNO electrode and C-FeTNO/rGO EPD electrode were left at open circuit for several months to ensure that the voltages were stabilized, showing 1.65 V (*vs.* Li/Li$^+$). After that, the coin cells were disassembled in an argon-filled glovebox and washed with a mixture of EC : DMC : DEC solvents, followed by drying inside a glovebox.

3. Results and discussion

3.1. Advanced TNO/graphene anode design

This research introduces a novel design concept of an advanced TNO/graphene composite electrode enabled by electrophoretic deposition. This novel electrode is made of a carbon-coated single-crystal Fe-substitution TNO material (C-FeTNO) and graphene oxide acting as a binder and conductive component.
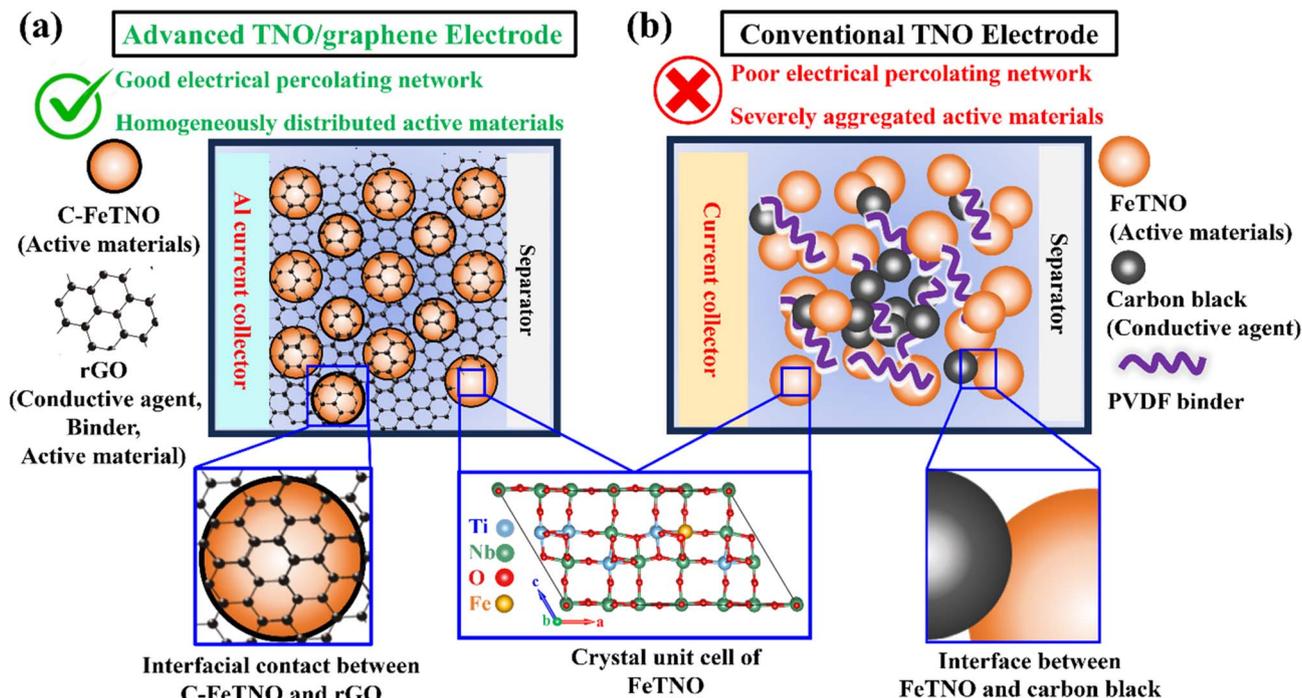
This journal is © The Royal Society of Chemistry 2025

J. Mater. Chem. A, 2025, **13**, 32207–32219 | **32209**

Fig. 1 Schematic illustration of the design of an advanced C-FeTNO/rGO electrode and its comparison to a conventional electrode.

This electrode is then processed by reductive annealing with hydrogen.

As shown in the graphical representation in Fig. 1(a), this advanced C-FeTNO/rGO EPD electrode consists of carbon-coated nanostructured Fe^{3+}-substitution TNO materials (C-FeTNO) and reduced graphene oxide (rGO), forming a binder-free all-active-material electrode. The advanced EPD electrode (Fig. 1(a)) is characterized by homogeneous distribution of the C-FeTNO nanomaterial component and the rGO multifunctional component. By contrast, the conventional LIB electrode (Fig. 1(b)) featuring the Fe-TNO active material, carbon black (conductive agent), and PVDF binder, assembled with the assistance of an organic solvent (e.g., N-methyl-2-pyrrolidone (NMP)) and deposited by doctor blading suffers from severe aggregation and a poor electrical percolating network. In both cases Al is used as the electron collector substrate.

3.2. Electrode engineering by EPD

To engineer the designed advanced electrode, we electrophoretically co-deposit GO and C-FeTNO from their suspension in isopropanol solvent employing LiOAc as a charging additive. Fig. 2(a) provides a schematic of the EPD cell.

3.2.1. Suspension formulation

3.2.1.1. Selection of organic solvents. Factors such as suspension stability, electrophoretic mobility, practical deposition rate, environmental friendliness, and potential health hazards need to be considered when selecting an optimal solvent. Given that C-FeTNO and GO are the main components, three benign organic solvents were short-listed as potential candidates, namely ethylene glycol, isopropanol, and ethanol,

after suspension media screening (detailed in the S2 Section of the SI). In stability testing, GO suspensions made with these solvents are highly stable (Fig. S1(a)), which arises from van der Waals interactions and hydrogen bonding between the oxygen-containing functional groups on GO and the organic molecules.[30] For C-FeTNO suspensions, the order of suspension stability (Fig. S1(b)) correlates strongly with solvent viscosity (Table S2): ethylene glycol (16.265 cP), isopropanol (2.044 cP), and ethanol (1.089 cP).[31,32] Although ethylene glycol yielded the most stable suspension, it was observed that the C-FeTNO particles have limited electrophoretic mobility (-0.215 μm cm V^{-1} s^{-1}, shown in Table S3) resulting in poor deposit formation. In contrast, the suspensions based on isopropanol and ethanol were found to exhibit good electrophoretic mobilities (-0.215 μm cm V^{-1} s^{-1} and -0.480 μm cm V^{-1} s^{-1}) and deposition rates. In particular, the isopropanol-based suspensions exhibited higher stability and more uniform deposition (Fig. S3) compared with ethanol-based suspensions. Therefore, isopropanol is deemed to be the optimal solvent for both C-FeTNO and GO.

3.2.1.2. Zeta potential measurements. The mean zeta potentials of isopropanol suspensions with C-FeTNO and GO (Fig. 2(b)) were determined to be -43 mV and -53 mV, respectively, indicating the presence of negative charge carriers on the surface of C-FeTNO and GO solids. It is noteworthy that the isopropanol-based suspension with C-FeTNO (with -45 mV) shows a higher absolute value of mean zeta potential than the ethanol-based suspension (with -35 mV) and ethylene glycol-based suspension (with -6 mV) as shown in Fig. S2, further confirming that isopropanol is the preferred solvent. The superior performance of isopropanol can be attributed to its
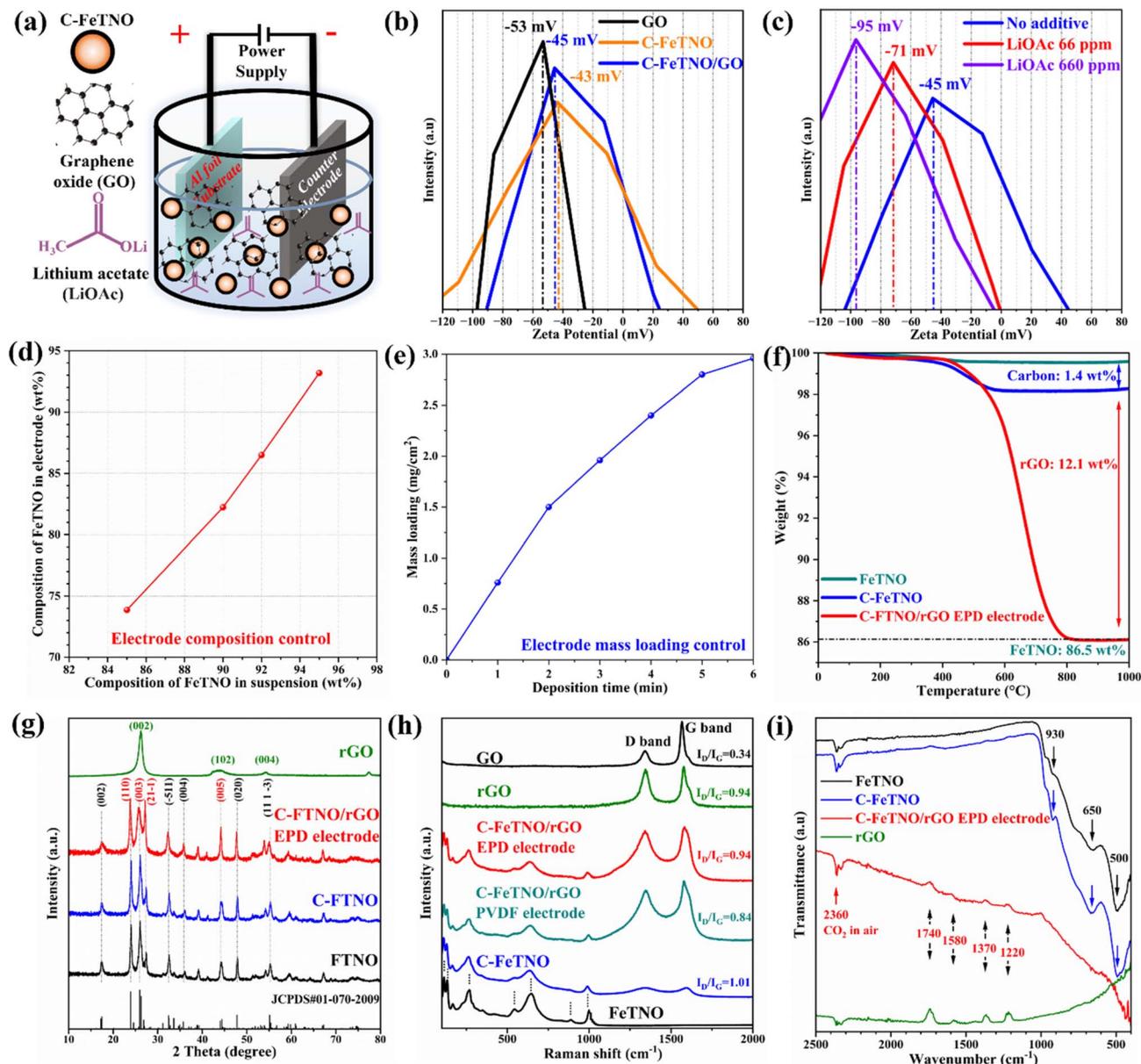
32210 | J. Mater. Chem. A, 2025, 13, 32207–32219

This journal is © The Royal Society of Chemistry 2025

Fig. 2 (a) Schematic illustration of the EPD cell, (b) zeta potential of C-FeTNO (2.76 g L^{-1}), GO (0.24 g L^{-1}), and C-FeTNO (2.76 g L^{-1})/GO (0.24 g L^{-1}) suspensions in isopropanol, (c) C-FeTNO/GO-isopropanol suspension with different concentrations of LiOAc additive (0 ppm, 66 ppm, and 660 ppm). (d) Composition of C-FeTNO/rGO EPD electrodes with varying suspension compositions. (e) Weight ratio of components determined by TGA. (f) Mass loading of the electrode with increasing EPD deposition time. (g) XRD patterns, (h) Raman spectra, and (i) FT-IR spectra of the FeTNO material, C-FeTNO material, C-FeTNO/rGO EPD electrode, and rGO material.

balanced properties: moderate viscosity, adequate electrophoretic mobility, and uniform deposition quality. From a fundamental aspect, this comparison between two polar solvents (isopropanol and ethanol)[31,32] provides deeper experimental insights: solvents with higher viscosity and lower polarity can tune particle mobility and stability, which results in more uniform and compact electrode deposition.

3.2.1.3. Effect of the charging agent. Lithium acetate (LiOAc) was added as a charging agent into the suspension to adjust the mean zeta potential and stabilize the suspension, thereby improving the uniformity of the EPD coating film.[33] Various concentrations (66 ppm and 660 ppm) of lithium acetate

(LiOAc) were used as additives in the C-FeTNO (2.76 g L^{-1})/GO (0.24 g L^{-1}) isopropanol suspension. The addition of LiOAc directly improved the suspension conductivity, absolute value of zeta potential, and electrophoretic mobilities, with these values increasing as the concentration increased (Table S5). Specifically, three suspensions with 0 ppm, 66 ppm, and 660 ppm LiOAc demonstrated zeta potentials of −45 mV, −71 mV, and −95 mV, respectively (Fig. 2(b)). These results can be attributed to the negative charge of acetate anions dominating the diffuse layer enwrapping the surface of C-FeTNO and GO. Consequently, the stabilized C-FeTNO/GO suspension with 66 ppm LiOAc yields a uniform deposition film (Fig. S3(d)). The

This journal is © The Royal Society of Chemistry 2025

J. Mater. Chem. A, 2025, **13**, 32207–32219 | **32211**

concentration of 660 ppm was not selected due to the potential risk of adding more impurity in the EPD film.

3.2.2. Electrophoretic deposition parameters. EPD parameters including applied electric field and suspension composition are controlled to optimize the deposit quality in terms of rate of deposition, composition, and mass loading. Given that the zeta potential of the suspension is negative, the electrode deposit forms on the anode and not the cathode. In other words, during EPD, the applied electric field transports negatively charged particles to the anode.

3.2.2.1. Applied electric field. During EPD, constant voltages of 50 V, 100 V, and 200 V were tested, all of which generate a high-quality deposition film. As illustrated in Fig. S4, uniform deposition is achieved across all samples deposited within the same deposition time (for 1 min). Increasing the deposition voltage enhances the deposition rate, resulting in higher deposited mass loadings: 0.75 mg cm^{-2} at 50 V, 1.07 mg cm^{-2} at 100 V, and 2.55 mg cm^{-2} at 200 V. However, the use of high voltages (*i.e.*, 100 V and 200 V) in the EPD process raises concerns regarding the oxidation of Al electrodes, as visualized by the slight change in surface appearance shown in Fig. S4. This observation is consistent with previous reports suggesting the increased risk of substrate oxidation, at elevated voltages during the EPD process.[33,34] Therefore, a low voltage of 50 V was chosen to avoid substrate oxidation under high voltages, even though 100 V and 200 V were found to have slightly higher deposition rates and efficiencies. Additionally, potential safety and health concerns associated with the use of higher voltages (*i.e.*, 100 V and 200 V) were also considered as a rationale for avoiding their application, as discussed in the SI.

3.2.2.2. Coating composition control. The composition ratio of C-FeTNO to GO in an EPD electrode can be adjusted by changing the suspension composition. The composition was determined *via* TGA measurements to reveal the correlation between suspension composition and electrode composition, as shown in Fig. 2(d). This allows precise targeting of the desired electrode composition to balance electronic conductivity (*i.e.*, rGO) and active material (*i.e.*, C-FeTNO). Eventually, the C-FeTNO/rGO electrode, consisting of 86.5 wt% FeTNO, 1.4 wt% carbon coating, and 12.1 wt% rGO (corresponding to a component ratio of 8 : 1 for C-FeTNO to rGO), was selected for comparison with the C-FeTNO/rGO/PVDF electrode prepared with a component weight ratio of 8 : 1 : 1.

3.2.2.3. Coating mass loading control. EPD allows for precise control over the mass loading on a substrate. By increasing deposition time by 1 minute per stage, mass loading can be adjusted from 0.25 up to 3.0 mg cm^{-2} within 6 min (Fig. 2(d)).

3.2.3. EPD electrode quality improvement. Fig. S5(a) compares the electrode quality of the EPD-assembled C-FeTNO/rGO binder-free electrode (EPD electrode) with the C-FeTNO/rGO/PVDF electrode fabricated *via* conventional tape casting (PVDF electrode). The EPD electrode exhibits a more homogeneous and smoother surface morphology than the PVDF electrode, contributing to a high-quality electrode interface. This improvement can be attributed to the advantage of nanoscale assembly during the electrophoretic deposition process,[19,35] although validation *via* mechanical adhesion strength testing

(S4 Section in the SI) needs further evaluation. Nevertheless, overall, the novel TNO-EPD electrode developed in this study demonstrates significant enhancement over the previous study of our group by Uceda *et al.*,[19] achieved through optimized solvent selection, advanced material design, and enhanced suspension control, as discussed in the S3 Section and summarized in Table S6.

3.3. Physical properties of the materials and electrode

The crystallographic properties of the FeTNO, C-FeTNO, C-FeTNO/rGO EPD electrode, and rGO were investigated by XRD analysis (Fig. 2(g)). The phase patterns of the FeTNO material, C-FeTNO material, and C-FeTNO/rGO EPD electrode can be indexed to the TiNb$_2$O$_7$ phase with a monoclinic C2/m space group (PDF#01-070-2009). Two predominant diffraction peaks of these three samples are positioned at 23.91° and 25.99° corresponding to the (110) and (003) lattice planes. The peak intensity ratio of (110)/(003) for the C-FeTNO/rGO EPD electrode differs from that of FeTNO and C-FeTNO materials, which can be attributed to the influence of XRD peaks associated with the (002) plane of rGO.[36]

Raman spectroscopy was carried out to determine the spectral features of carbon (GO, rGO, and surface carbon) and FeTNO samples. As shown in Fig. 2(h), two prominent peaks, the D band and G band, are positioned at ~1320–1350 cm^{-1} and ~1570–1605 cm^{-1}, which can be attributed to the vibrations of disordered carbon and ordered graphitic carbon, respectively.[37,38] The peak intensity ratio of the D band to G band (I_D/I_G) of the rGO sample ($I_D/I_G = 0.94$) and the C-FeTNO/rGO EPD electrode ($I_D/I_G = 0.94$) is higher than that of GO ($I_D/I_G = 0.33$), suggesting that GO is successfully reduced to rGO.[39,40] The increase of the D band signal is likely due to more local defects and disorders, formed due to the deoxygenation of GO.[40] By contrast, the C-FeTNO/rGO PVDF electrode sample illustrates a lower I_D/I_G value ($I_D/I_G = 0.84$), as some of the graphene layers in the rGO sample are re-oxidized by oxygen-containing groups during the tape casting approach.[22] This comparative Raman analysis in Fig. 2(h) suggests the EPD method is more effective than traditional tape casting (PVDF method) at preventing the oxidation of graphene. Meanwhile, the peaks of the D band and G band that emerge in the C-FeTNO sample ($I_D/I_G = 1.01$) can be ascribed to the surface carbon coated on the FeTNO particles.[17,41] For the C-FeTNO and C-FeTNO/rGO EPD electrodes, the peaks observed at <1200 cm^{-1} align closely with those of TiNb$_2$O$_7$ samples reported previously.[42–44] Specifically, the two peaks at 988 cm^{-1} and 880 cm^{-1} originate from the vibrations of the edge and corner-shared NbO$_6$ octahedra, respectively.[42,43] The peaks at 635 cm^{-1} and 540 cm^{-1} are indicative of the vibrations of the edge- and corner-shared TiO$_6$ octahedra, respectively. Additionally, the peaks at 263 cm^{-1} and 163 cm^{-1} are associated with vibrations of complex models that include the antisymmetric and symmetric bending vibrations of O–Nb–O and O–Ti–O.[45]

FT-IR spectra (Fig. 2(i)) were obtained to further confirm the bonding environment of the C-TNO/rGO composite anode. The bands at approximately 500 cm^{-1} and 930 cm^{-1} arise from the

32212 | *J. Mater. Chem. A*, 2025, **13**, 32207–32219

This journal is © The Royal Society of Chemistry 2025

stretching vibrations of the Nb–O–Nb bridging bonds and Nb–O bonds, respectively.[46] The absorption peak at 650 cm^{-1} is attributed to the stretching vibration of Ti–O–Ti bonds.[47] The peak at 2360 cm^{-1} is associated with CO_2 in air.[18] Additionally, the FT-IR spectra revealed the nature of the functional groups in GO and C-FeTNO/rGO EPD electrodes. The absorption peaks at 1740 cm^{-1}, 1580 cm^{-1}, 1370 cm^{-1}, and 1220 cm^{-1} are attributed to C=O stretching, C=C stretching, C–O–H bending, and C–O stretching, respectively.[48] The peak signals corresponding to these functional groups were decreased in intensity, which likely suggests the successful reduction of GO to rGO.[48] Overall, both Raman and FT-IR spectra consistently confirm that GO is successfully converted to rGO by the H_2-reductive annealing process, while the properties of FeTNO and C-FeTNO remain unchanged.

3.4. Morphological structure of the C-FeTNO material and C-FeTNO/rGO-EPD electrode

Fig. 3 presents the morphological features of the C-FeTNO material and C-FeTNO/rGO EPD electrode. The SEM image (Fig. 3(a)), TEM image (Fig. 3(b)), and HAADF image (Fig. 3(c)) reveal C-FeTNO to be in the form of nanometric single crystals with size ranging from 20–100 nm. The single crystal structure of C-FeTNO is verified by the interlayer spacing of 1.04 nm correponding to the (001) plane (d_{001}) of $TiNb_2O_7$, as shown in Fig. 3(d). Additionally, the carbon layer coated on C-FeTNO has a thickness of 1.32 nm. EDS mapping (Fig. 3(e)) reveals that Ti (Fig. 3(g)), Nb (Fig. 3(h)), O (Fig. 3(i)), and Fe (Fig. 3(j)) elements are homogeneously distributed within the bulk of C-FeTNO, while the C element (Fig. 3(f)) is evenly distributed on the surface of FeTNO. Furthermore, the microstructure of the C-FeTNO/rGO EPD electrode (Fig. 3(k–t)) has been investigated. As shown in Fig. 3(k–m), C-FeTNO particles are successfully assembled into a three-dimensional rGO composite structure. The corresponding SAED image (Fig. 3(n)) illustrates the periodic arrangements characteristic of C-FeTNO/rGO composite materials, aligning with the monocrystalline nature of FeTNO and the few-layer structure of rGO. The uniform distribution of C (Fig. 3(p)), Ti (Fig. 3(q)), Nb (Fig. 3(r)), O (Fig. 3(s)), and Fe (Fig. 3(t)) elements is demonstrated by EDS mapping (Fig. 3(o)). The obtained C-FeTNO/rGO EPD electrode features
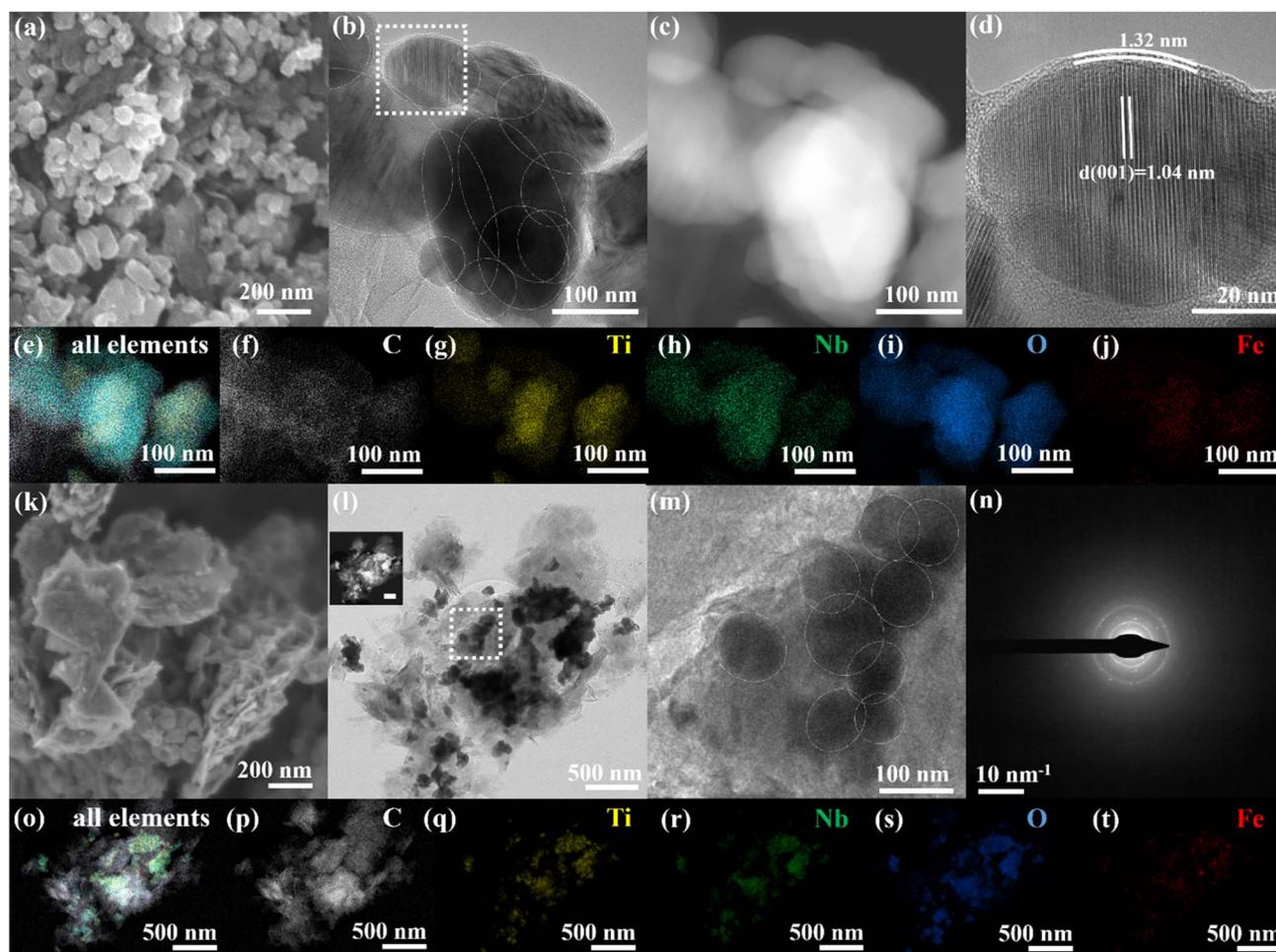

Fig. 3 C-FeTNO material: (a) SEM image, (b) TEM image, (c) HAADF image, (d) HRTEM image of the selected area, and EDX elemental mapping showing (e) all elements, (f) C, (g) Ti, (h) Nb, (i) O, and (j) Fe. C-FeTNO/rGO EPD electrode: (k) SEM image, (l) TEM image with inserted HAADF image, (m) HRTEM image of the selected area, (n) SAED image, and EDX elemental mapping showing (o) all elements, (p) C, (q) Ti, (r) Nb, (s) O, and (t) Fe.

This journal is © The Royal Society of Chemistry 2025

J. Mater. Chem. A, 2025, **13**, 32207–32219 | **32213**

nanostructured C-FeTNO homogeneously embedded between graphene sheets, which realizes the concept design demonstrated in Fig. 1.

3.5. Electrode homogeneity and microstructure

The electrode homogeneity and interfacial contact were investigated through cross-sectional SEM imaging (Fig. 4(a, c and e)) and elemental mapping of C, Ti, Nb, and O (Fig. 4(b, d and f)). Fig. 4(a and b) reveals that C-FeTNO and rGO materials are homogeneously distributed within the C-FeTNO/rGO EPD electrode, suggesting the formation of a uniform three-dimensional percolation network, which is instrumental in constructing ultrafast electronic and ionic conduction pathways. These desirable characteristics of advanced electrodes can be attributed to the remarkable submicron/nanoscale self-assembly and deposition capability of the EPD technique.[25] By contrast, the conventional tape casting method is limited by non-homogeneous deposition and aggregation of nanomaterials. For example, the C-FeTNO/rGO PVDF electrode (Fig. 4(c and d)) and C-FeTNO/CB PVDF electrode (Fig. 4(e and f)) demonstrate severe aggregation of C-FeTNO and conductive carbon (rGO and CB) materials, indicating non-uniform composition in the bulk or interface of the electrode.

3.6. Electrochemical performance

The influence of the advanced electrode microstructure on interface impedance (Fig. 5(a)) and redox overpotential (Fig. 5(b)) was investigated by EIS and CV measurements of the C-FeTNO/rGO EPD electrode, C-FeTNO/rGO PVDF electrode, C-FeTNO electrode, and FeTNO electrode, respectively. The EIS circuit model is shown in Fig. S12. As illustrated in Fig. 5(a), the charge transfer resistance (R_{CT}) of the pristine electrode (without lithiation) for the FeTNO electrode is measured to be 183 ohms. In contrast, the R_{CT} of the C-FeTNO electrode is reduced to 132 ohms, suggesting the surface carbon coating improves the electronic conductivity of the electrode. Most notably, the C-FeTNO/rGO EPD electrode exhibits the lowest R_{CT} (only 75 ohms) among all electrodes tested, which can be attributed to the highly-conductive rGO network and homogeneous electrode interphase enabled by the optimized EPD technique. Conversely, the C-FeTNO/rGO PVDF electrode has the highest R_{CT} of 241 ohms. This is likely because part of the rGO material in the electrode has been oxidized back to GO, a low-conductivity phase, during the conventional electrode procedure, as revealed by the Raman spectra (Fig. 2(h)). The significant difference in R_{CT} between the C-FeTNO/rGO EPD electrode and C-FeTNO/rGO PVDF electrode highlights the superiority of the EPD electrode fabrication method over the conventional PVDF approach in constructing electrodes with high conductivity and superior interface contact for TNO/graphene composite electrodes. A similar trend is observed with CV data in Fig. 5(b); the graphene 3D electrode network enabled by the EPD technique promotes the depolarizing effect of the TNO-based electrode during lithiation and delithiation. For example, the C-FeTNO/rGO EPD electrode, with a cathodic potential of 1.60 V and anodic potential of 1.70 V (Fig. 5(b)), has a smaller anodic and cathodic overpotential than C-FeTNO and FeTNO electrodes, respectively, compared with the equilibrium potential of 1.65 V for the TNO-based electrode.[7] In addition, the Li-ion diffusion coefficient ($D_{Li^+,GITT}$) was calculated by GITT curves and eqn (S1).[49,50] The $D_{Li^+,GITT}$ of the C-FeTNO/rGO EPD electrode is determined to be from 5.5×10^{-12} to 1.5×10^{-11} cm^2 s^{-1} during charging (Fig. 5(d)) and from 2.9×10^{-12} to 1.1
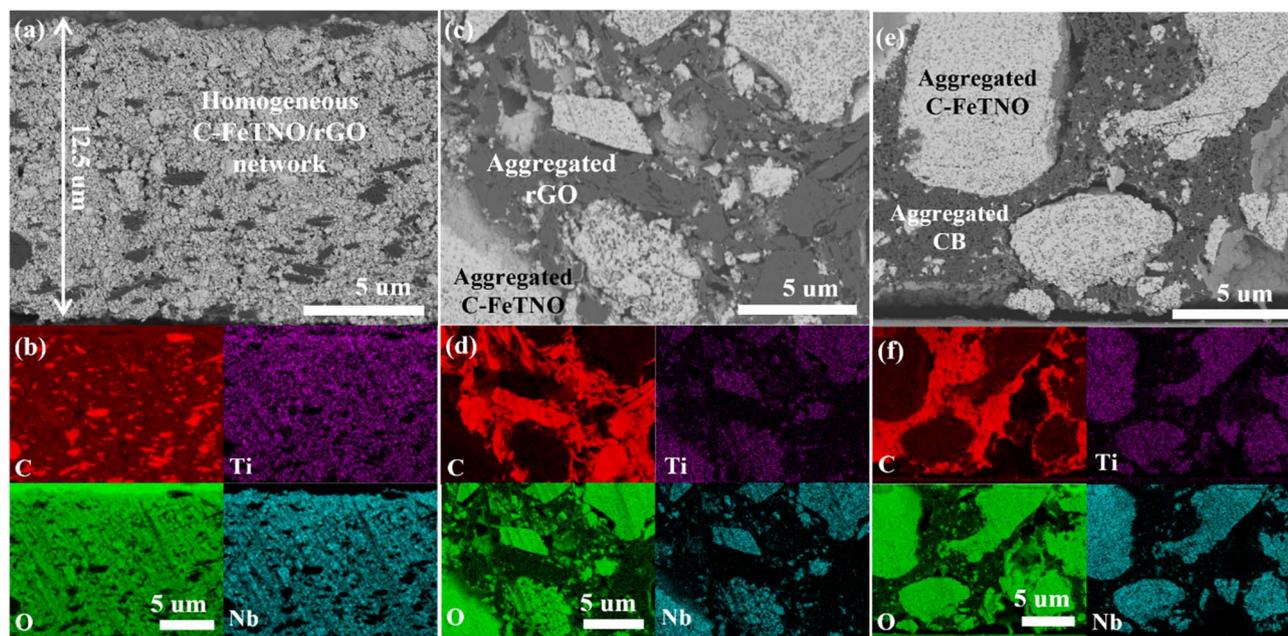

Fig. 4 (a) Cross-sectional SEM image and (b) EDS mapping of the C-FeTNO/rGO EPD electrode. (c) Cross-sectional SEM image and (d) EDS mapping of the C-FeTNO/rGO PVDF electrode. (e) Cross-sectional SEM image and (f) EDS mapping of the C-FeTNO electrode.
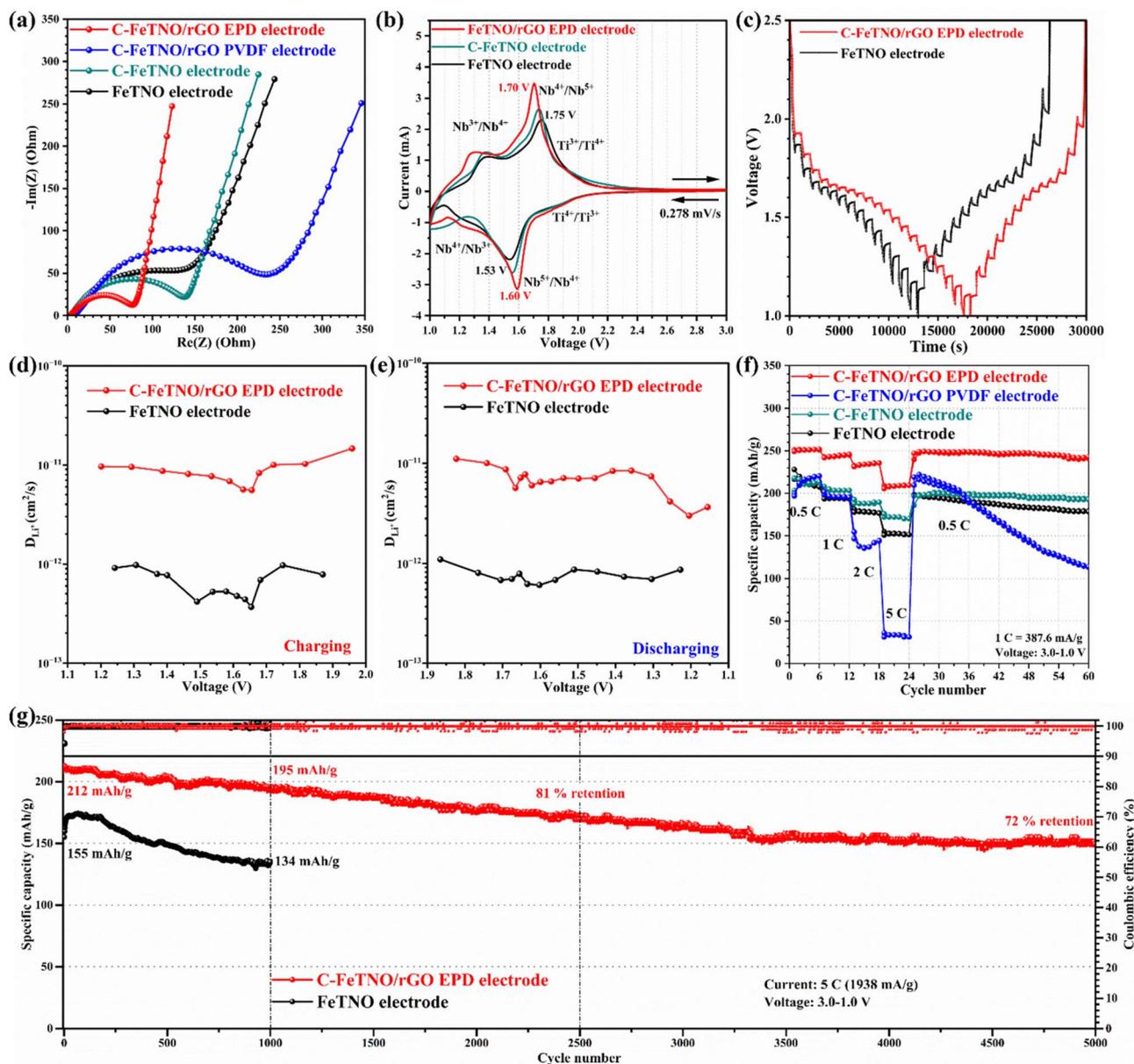
32214 | J. Mater. Chem. A, 2025, **13**, 32207–32219

This journal is © The Royal Society of Chemistry 2025

Fig. 5 (a) EIS, (b) CV, (c) GITT and D_{Li^+} of the C-FeTNO/rGO EPD electrode and the FeTNO electrode during (d) charging and (e) discharging. (f) Rate performance of the C-FeTNO/rGO EPD electrode, C-FeTNO/rGO PVDF electrode, C-FeTNO electrode, and FeTNO electrode, (g) long cycling performance of the C-FeTNO/rGO EPD electrode and the FeTNO electrode.

$\times 10^{-11}$ cm^2 s^{-1} during discharging (Fig. 5(e)). These results are an order of magnitude higher than those of the FeTNO electrode, ranging from 3.7×10^{-13} to 9.8×10^{-13} cm^2 s^{-1} during charging (Fig. 5(d)) and from 6.1×10^{-13} to 1.1×10^{-12} cm^2 s^{-1} during discharging (Fig. 5(e)). Also, the Li-ion diffusion coefficient ($D_{Li^+,PITT}$) was determined by the potentiostatic intermittent titration technique (PITT) (Fig. S11(a and b)), according to eqn (S1) and (S2). As illustrated in Fig. S11(c and d), the C-FeTNO/rGO EPD electrode exhibits significantly higher $D_{Li^+,PITT}$ values, ranging from 1.1×10^{-12} to 4.5×10^{-11} cm^2 s^{-1}. These values are approximately an order of magnitude higher that those observed for the FeTNO electrode (1.1×10^{-13} to 1.7

$\times 10^{-12}$ to cm^2 s^{-1}), consistent with the results from GITT measurements.

The lithium storage performance of the fabricated electrodes was tested under galvanostatic cycling in the voltage window from 3 V to 1 V. It is worth noting that all the capacity calculations are based on the mass of the electrode, including both active materials, binder, and conductive agent. Fig. 5(f) demonstrates rate performances of the C-FeTNO/rGO EPD electrode, C-FeTNO/rGO PVDF electrode, C-FeTNO electrode, and FeTNO electrode. The FeTNO electrode offers capacities of 228, 200, 180, and 156 mAh g^{-1} at 0.5C, 1C, 2C, and 5C, respectively. In contrast, the C-FeTNO electrode provides 218,

This journal is © The Royal Society of Chemistry 2025

J. Mater. Chem. A, 2025, 13, 32207–32219 | 32215

208, 192, and 176 mAh g^{-1} at the same rates, illustrating improved rate performance due to the conductive carbon coating layer. Notably, the C-FeTNO/rGO EPD electrode displays the best rate performance, demonstrating 252, 246, 236, and 210 mAh g^{-1} at 0.5C, 1C, 2C, and 5C, and shows superior recyclability (248 mAh g^{-1}) at 0.5C after rate testing. In contrast, the C-FeTNO/rGO PVDF electrode (conventional electrode) illustrates poor rate performance of 220, 201, 140, and 32 mAh g^{-1} at 0.5C, 1C, 2C, and 5C, respectively, demonstrating a severe capacity drop. This battery failure is likely due to severe aggregation of electrode materials (Fig. 4(c)) and the oxidation of rGO in the C-FeTNO/rGO PVDF electrode, aligning with the findings in the EIS results (Fig. 5(a)).

Accordingly, the optimal EPD electrode was selected to further investigate the battery cycling stability under the galvanostatic cycling at 5C. The C-FeTNO/rGO EPD electrode
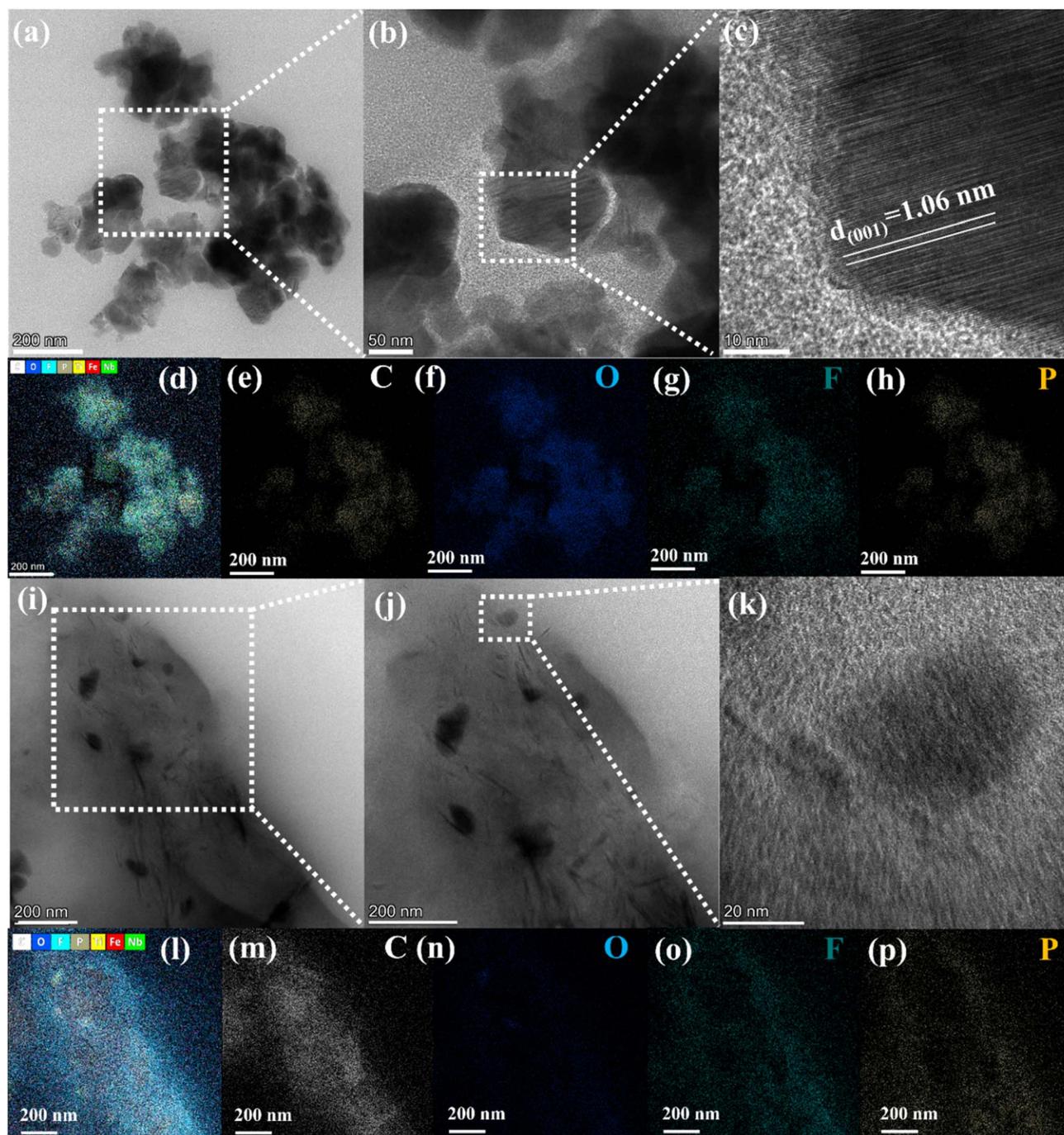

Fig. 6 Post-mortem TEM analysis of cycled FeTNO materials: (a and b) TEM images, (c) HRTEM image. EDX elemental mapping showing the distribution of (d) all elements, (e) C, (f) O, (g) F, and (h) P post-mortem TEM analysis of the cycled C-FeTNO/rGO EPD electrode: (i and j) TEM images, (k) HRTEM image. EDX elemental mapping showing the distribution of (l) all elements, (m) C, (n) O, (o) F, and (p) P.

32216 | J. Mater. Chem. A, 2025, 13, 32207–32219

This journal is © The Royal Society of Chemistry 2025

(Fig. 5(g)) provides high capacities of 212 mAh g^{-1} at the 1st cycle and 195 mAh g^{-1} at the 1000th cycle at 5C and illustrates high retentions of 81% at the 2500th cycle and 72% after 5000 cycles, outperforming the FeTNO electrode (Fig. 5(g)). This result is consistent with the observations in the EIS data (Fig. 5(a)), CV data (Fig. 5(b)), and $D_{Li^+,GITT}$ results (Fig. 5(d and e)). The remarkable electrochemical performance of the advanced C-FeTNO/rGO EPD electrode demonstrates the advantage of advanced electrode engineering *via* the EPD technique in constructing a uniform interphase and functional electrode. It benefits from synergy strategies of carbon coating and a graphene three-dimensional network, compared with conventional electrode engineering.

To investigate the morphological and interfacial evolution of electrode materials after prolonged cycling, post-mortem TEM analysis was performed after 5000 cycles at 5C, corresponding to Fig. 5(g). As shown in the TEM images (Fig. 6(a and b)), the cycled FeTNO particles retain their nanostructured morphology, exhibiting no visible structural changes or cracking compared to Fig. 3(b), which implies their stable intrinsic stability. Fig. 6(c) provides more details of single-crystal structure and reveals that the interlayer spacing of the (001) plane has expanded to 1.06 nm due to lithium insertion, which is slightly larger than the 1.04 nm observed in the pristine material shown in Fig. 3(d). The EDS mapping images in Fig. 6(d–h), S8, and S9 illustrate the presence of Fe, Ti, Nb, O, C, fluorine (F) and phosphorus (P) elements in the C-FeTNO electrode. Interestingly, F and P elements are distributed on the surface of FeTNO, as shown in Fig. 6(e), which suggests the formation of the solid electrolyte interphase (SEI) after prolonged lithiation–delithiation reactions.[51,52] The formation and growth of a low-conductivity SEI at the interface of the active material reduces the electronic mobility apparently contributing to the observed electrode failure as depicted in Fig. 5(g).[51,52]

By contrast, in the C-FeTNO/rGO electrode, the C-FeTNO is embedded between the reduced graphene oxide (rGO) layers as illustrated in TEM images (Fig. 6(i–k)), HAADF image (Fig.S10(a)), and Fe, Ti, and Nb mapping (Fig. S10(b–i)). Additionally, the fluorine (F) and phosphorus (P) elements are co-localized with carbon as illustrated in Fig. 6(i, j) and S10(h, i), suggesting that the SEI film forms primarily on the surface of the rGO. This rGO layer likely acts as a protective barrier, preventing direct SEI formation on the active material surface, providing a highly conductive network and thereby enhancing the cycling stability of the C-FeTNO/rGO electrode. Overall, this electrode design offers significant advantages in favorably modifying the interfacial structure, thereby maintaining a fast kinetic pathways for both electrons and ions.

4. Conclusion

In summary, we developed an advanced EPD-based electrode engineering technique to fabricate Fe-doped single-crystal TNO nanomaterial (FeTNO)/reduced graphene oxide (rGO) composite materials for binder-free LIB electrodes. The novel EPD engineered anodes are characterized by a homogeneous

electrode microstructure and well-defined interfacial contact within the FeTNO/rGO 3D network, as evidenced by its morphological and composition analysis. Additionally, this advanced EPD approach effectively addresses the re-oxidation of rGO and its severe aggregation typically observed in conventional electrode fabrication. Consequently, the C-FeTNO/rGO EPD electrode provides a low impedance of 75 ohms compared with that of the C-FeTNO/rGO PVDF electrode (241 ohms) and FeTNO electrode (183 ohms). The FeTNO/rGO EPD electrode provides remarkable capacity and rate capability: 252, 246, 236, and 210 mAh g^{-1} at 0.5C, 1C, 2C, and 5C. Additionally, it offers an exceptional long-cycling performance with 81% retention (initial capacity of 212 mAh g^{-1}) at the 2500th cycle and 72% after 5000 cycles at 5C, making it a strong ultrafast-charging and safe LIB anode. The remarkable battery performance can be attributed to advanced electrode engineering and interphase control endowed by the synergy of EPD's nanoscale assembly power, reduced graphene oxide network, carbon coating, and substitutional doping of TNO nanomaterials. These findings offer valuable insights into TiNb$_2$O$_7$ as a promising alternative anode material for ultrafast-charging applications.

Author contributions

Fan Yu: conceptualization, methodology, investigation, formal analysis, validation, data curation, software, visualization, writing – original draft, writing – review & editing. Yihan Wang: investigation, writing – review & editing. Nicolas Brodusch: investigation, formal analysis. Bobby Miglani: writing – review & editing. Nauman Mubarak: peel adhesive testing. Prof. Jinhyuk Lee: formal analysis and peel adhesive testing. Prof. Raynald Gauvin: formal analysis. Prof George P. Demopoulos: funding acquisition, supervision, conceptualization, methodology, formal analysis, writing – review & editing.

Conflicts of interest

There are no conflicts of interest to declare.

Data availability

The data supporting this article have been included as part of the SI. See DOI: **https://doi.org/10.1039/d5ta03042k**.

Acknowledgements

This journal is © The Royal Society of Chemistry 2025

J. Mater. Chem. A, 2025, **13**, 32207–32219 | **32217**

conducting the trial and initial investigation of *in situ* XRD testing for this research. F. Y. extends thanks to Petr Fiurasek and McGill Chemistry Characterization Facility for their support with TGA and Raman testing.

References

1 Y. Liu, Y. Zhu and Y. Cui, *Nat. Energy*, 2019, **4**, 540–550.

2 W. Zhang, D.-H. Seo, T. Chen, L. Wu, M. Topsakal, Y. Zhu, D. Lu, G. Ceder and F. Wang, *Science*, 2020, **367**, 1030–1034.

3 J. W. Choi and D. Aurbach, *Nat. Rev. Mater.*, 2016, **1**, 16013.

4 C. Guo, Z. Liu, K. Han, L. Zhang, X. Ding, X. Wang and L. Mai, *Small*, 2022, **18**, 2107365.

5 X. Lu, L. Gu, Y. S. Hu, H. C. Chiu, H. Li, G. P. Demopoulos and L. Q. Chen, *J. Am. Chem. Soc.*, 2015, **137**, 1581–1586.

6 H. C. Chiu, X. Lu, J. Zhou, L. Gu, J. Reid, R. Gauvin, K. Zaghib and G. P. Demopoulos, *Adv. Energy Mater.*, 2017, **7**, 1601825.

7 K. J. Griffith, Y. Harada, S. Egusa, R. M. Ribas, R. S. Monteiro, R. B. Von Dreele, A. K. Cheetham, R. J. Cava, C. P. Grey and J. B. Goodenough, *Chem. Mater.*, 2021, **33**, 4–18.

8 Y. Yang and J. Zhao, *Adv. Sci.*, 2021, **8**, 2004855.

9 X. Wu, S. Lou, X. Cheng, C. Lin, J. Gao, Y. Ma, P. Zuo, C. Du, Y. Gao and G. Yin, *ACS Appl. Mater. Interfaces*, 2018, **10**, 27056–27062.

10 S. Gong, Y. Wang, Q. Zhu, M. Li, Y. Wen, H. Wang, J. Qiu and B. Xu, *J. Power Sources*, 2023, **564**, 232672.

11 C. Yang, D. Ma, J. Yang, M. Manawan, T. Zhao, Y. Feng, J. Li, Z. Liu, Y.-W. Zhang, R. B. Von Dreele, B. H. Toby, C. P. d. L. Albarrán and J. H. Pan, *Adv. Funct. Mater.*, 2023, **33**, 2212854.

12 K. J. Griffith, I. D. Seymour, M. A. Hope, M. M. Butala, L. K. Lamontagne, M. B. Preefer, C. P. Koçer, G. Henkelman, A. J. Morris, M. J. Cliffe, S. E. Dutton and C. P. Grey, *J. Am. Chem. Soc.*, 2019, **141**, 16706–16725.

13 H. Wang, R. Qian, Y. Cheng, H.-H. Wu, X. Wu, K. Pan and Q. Zhang, *J. Mater. Chem. A*, 2020, **8**, 18425–18463.

14 F. Yu, S. Wang, R. Yekani, A. La Monaca and G. P. Demopoulos, *J. Energy Storage*, 2024, **95**, 112482.

15 L. Hu, L. J. Luo, L. F. Tang, C. F. Lin, R. J. Li and Y. J. Chen, *J. Mater. Chem. A*, 2018, **6**, 9799–9815.

16 F. Yu, B. Miglani, S. Yuan, R. Yekani, K. H. Bevan and G. P. Demopoulos, *Nano Energy*, 2025, **133**, 110494.

17 C. Wang, Z. Guo, W. Shen, Q. Xu, H. Liu and Y. Wang, *Adv. Funct. Mater.*, 2014, **24**, 5511–5521.

18 W. Chung and J. H. Bang, *ACS Appl. Mater. Interfaces*, 2022, **14**, 19365–19375.

19 M. Uceda, H.-C. Chiu, J. Zhou, R. Gauvin, K. Zaghib and G. P. Demopoulos, *Nanoscale*, 2020, **12**, 23092–23104.

20 R. Raccichini, A. Varzi, S. Passerini and B. Scrosati, *Nat. Mater.*, 2015, **14**, 271–279.

21 J. Q. Zhou, H. Y. Dong, Y. Chen, Y. H. Ye, X. Liao, B. H. Deng and J. P. Liu, *Chem. Commun.*, 2021, **57**, 1822–1825.

22 C. Vallés, C. Drummond, H. Saadaoui, C. A. Furtado, M. He, O. Roubeau, L. Ortolani, M. Monthioux and A. Pénicaud, *J. Am. Chem. Soc.*, 2008, **130**, 15802–15804.

23 N. Takami, K. Ise, Y. Harada, T. Iwasaki, T. Kishi and K. Hoshina, *J. Power Sources*, 2018, **396**, 429–436.

24 M. Léger, A. La Monaca, N. Basu and G. P. Demopoulos, *Next Sustain.*, 2025, **5**, 100084.

25 M. Diba, D. W. H. Fam, A. R. Boccaccini and M. S. P. Shaffer, *Prog. Mater. Sci.*, 2016, **82**, 83–117.

26 L. H. Ye, K. C. Wen, Z. X. Zhang, F. Yang, Y. C. Liang, W. Q. Lv, Y. K. Lin, J. M. Gu, J. H. Dickerson and W. D. He, *Adv. Energy Mater.*, 2016, **6**, 1502018.

27 S. J. Limmer and G. Z. Cao, *Adv. Mater.*, 2003, **15**, 427–431.

28 M.-J. Hwang, M.-G. Kim, S. Kim, Y. C. Kim, H. W. Seo, J. K. Cho, I.-K. Park, J. Suhr, H. Moon, J. C. Koo, H. R. Choi, K. J. Kim, Y. Tak and J.-D. Nam, *Carbon*, 2019, **142**, 68–77.

29 Y. H. Lu, D. W. Zhang, L. Wang, M. W. Xu, J. Song and J. B. Goodenough, *J. Electrochem. Soc.*, 2012, **159**, A321–A324.

30 V. V. Neklyudov, N. R. Khafizov, I. A. Sedov and A. M. Dimiev, *Phys. Chem. Chem. Phys.*, 2017, **19**, 17000–17008.

31 P. Amrollahi, J. S. Krasinski, R. Vaidyanathan, L. Tayebi and D. Vashaee, in *Handbook of Nanoelectrochemistry: Electrochemical Synthesis Methods, Properties, and Characterization Techniques*, ed. M. Aliofkhazraei and A. S. H. Makhlouf, Springer International Publishing, Cham, 2016, pp. 561–591.

32 Z. Mousavi, M. Pirdashti, A. A. Rostami and E.-N. Dragoi, *Int. J. Thermophys.*, 2020, **41**, 19.

33 R. J. Mou, S. Barua, A. K. Prasad, T. H. Epps III and K. P. C. Yao, *ACS Appl. Mater. Interfaces*, 2024, **16**, 6908–6919.

34 W. J. Stępniowski and Z. Bojar, in *Handbook of Nanoelectrochemistry: Electrochemical Synthesis Methods, Properties, and Characterization Techniques*, ed. M. Aliofkhazraei and A. S. H. Makhlouf, Springer International Publishing, Cham, 2016, pp. 593–645, DOI: 10.1007/978-3-319-15266-0_19.

35 M. Uceda, H.-C. Chiu, R. Gauvin, K. Zaghib and G. P. Demopoulos, *Energy Storage Mater.*, 2020, **26**, 560–569.

36 Z. Y. Xia, S. Pezzini, E. Treossi, G. Giambastiani, F. Corticelli, V. Morandi, A. Zanelli, V. Bellani and V. Palermo, *Adv. Funct. Mater.*, 2013, **23**, 4684–4693.

37 Y. Yang, J. Q. Li, D. Q. Chen and J. B. Zhao, *ACS Appl. Mater. Interfaces*, 2016, **8**, 26730–26739.

38 B. Lesiak, G. Trykowski, J. Tóth, S. Biniak, L. Kövér, N. Rangam, L. Stobinski and A. Malolepszy, *J. Mater. Sci.*, 2021, **56**, 3738–3754.

39 K. Zhao, L. Zhang, R. Xia, Y. Dong, W. Xu, C. Niu, L. He, M. Yan, L. Qu and L. Mai, *Small*, 2016, **12**, 588–594.

40 R. Sun, Q. Wei, Q. Li, W. Luo, Q. An, J. Sheng, D. Wang, W. Chen and L. Mai, *ACS Appl. Mater. Interfaces*, 2015, **7**, 20902–20908.

41 D. Liang, Y. Lu, N. Zhou and Z. Xu, *Nanomaterials*, 2022, **12**(17), 2943.

42 N. G. Eror and U. Balachandran, *J. Solid State Chem.*, 1982, **45**, 276–279.

43 L. Perfler, V. Kahlenberg, C. Wikete, D. Schmidmair, M. Tribus and R. Kaindl, *Inorg. Chem.*, 2015, **54**, 6836–6848.

44 A. W. Bayeh, D. M. Kabtamu, Y.-C. Chang, G.-C. Chen, H.-Y. Chen, G.-Y. Lin, T.-R. Liu, T. H. Wondimu, K.-C. Wang and C.-H. Wang, *J. Mater. Chem. A*, 2018, **6**, 13908–13917.

32218 | *J. Mater. Chem. A*, 2025, **13**, 32207–32219

This journal is © The Royal Society of Chemistry 2025

45 Y. Yang, J. Huang, Z. Cao, Z. Lv, D. Wu, Z. Wen, W. Meng, J. Zeng, C. C. Li and J. Zhao, *Adv. Sci.*, 2022, **9**, 2104530.

46 S. F. Lou, X. Q. Cheng, Y. Zhao, A. Lushington, J. L. Gao, Q. Li, P. J. Zuo, B. Q. Wang, Y. Z. Gao, Y. L. Ma, C. Y. Du, G. P. Yin and X. L. Sun, *Nano Energy*, 2017, **34**, 15–25.

47 W. Cai, G. Lu, J. He and Y. Lan, *Ceram. Int.*, 2012, **38**, 3167–3174.

48 L. Rout, A. Kumar, R. S. Dhaka, G. N. Reddy, S. Giri and P. Dash, *Appl. Catal., A*, 2017, **538**, 107–122.

49 Y. Zeng, H.-C. Chiu, B. Ouyang, K. Zaghib and G. P. Demopoulos, *ACS Appl. Energy Mater.*, 2020, **3**, 675–686.

50 H. Park, H. B. Wu, T. Song, X. W. Lou and U. Paik, *Adv. Energy Mater.*, 2015, **5**, 1401945.

51 K. Xu, *Chem. Rev.*, 2014, **114**, 11503–11618.

52 K. Xu, *Chem. Rev.*, 2004, **104**, 4303–4418.

This journal is © The Royal Society of Chemistry 2025

J. Mater. Chem. A, 2025, **13**, 32207–32219 | **32219**